# Three-Dimensional Modeling of Turbid Density Currents in Imha Reservoir, South Korea

Sangdo An[1] and Pierre Y. Julien, M.ASCE[2]

**Abstract:** The propagation dynamics of the turbid density currents of the Imha Reservoir is investigated using the FLOW-3D computational fluid dynamics code. The renormalization group (RNG) $\kappa$-$\varepsilon$ turbulence scheme in a Reynolds-averaged Navier–Stokes (RANS) framework was applied for the field investigation. A new particle dynamics algorithm was developed and coupled with the FLOW-3D model to simulate the settling of sediment particles, and the model was tested with field measurements during Typhoon Ewiniar. The coupled model correctly predicted the spatial and temporal evolution of intrusive density currents with plunging flows at a depth of 20 m and interflows propagating downstream at about 0.2 m/s. The simulation results with sediment settling demonstrated that the ratio of transported to initial sediment concentration ($C_0/C_i$) varies as a function of particle size $d_s$ and sediment concentration. Density currents can be classified into three regimes: (1) a suspended regime ($d_s < 10$ $\mu$m), where interflows will transport most of the sediment inflows from the reservoir inlet to Imha Dam; (2) a transition regime (10 $\mu$m $< d_s <$ 40 $\mu$m), where deposition rates alter the flow dynamics; and (3) a deposition regime ($d_s > 40$ $\mu$m), where sediment particles rapidly settle out without forming a density current. For the suspended regime, river inflows will define three different types of density currents in the reservoir: (1) interflows when $C_i < 2{,}000$ mg/L; (2) multiple intrusions when $2{,}000 < C_i < 3{,}000$ mg/L; and (3) plunging underflows when $C_i > 3{,}000$ mg/L. **DOI: 10.1061/(ASCE)HY.1943-7900.0000851.** 

**Author keywords:** Density currents; Turbidity; Stratified flow; Reservoirs; Sediment transport; Settling velocity; Computational fluid dynamics; Turbid density currents; Imha Dam.



## Introduction

Severe floods can trigger the intrusion of highly turbid waters into reservoirs from significant amounts of suspended sediments. The settling of suspended sediment reduces the capacity of reservoirs and degrades their water quality (Morris and Fan 1998; Julien 2010). Very fine sediment particles transported into reservoirs can also increase turbidity levels for extended periods of time and thus result in the deterioration of water quality. High turbidity levels that persist over long periods of time can increase the cost of water treatment and can cause permanent damage to downstream ecosystems (Chikita and Okumura 1990; Chung et al. 2009; Umeda et al. 2006). In South Korea, the most severe rainfall events occur during the summer typhoon season. For instance, Imha Reservoir has suffered from long periods of time with turbidity levels in excess of 880 NTU (An 2011), as shown in Fig. 1.

Beside erosion control at the watershed scale, an effective method for controling the release of highly turbid waters below reservoirs is based on the selective discharge of turbid waters by an intake facility with multiple intake elevations (Lee et al. 2007). Alternatively, the construction of solid or permeable obstacles such as submerged weirs or geotextile screens (De Cesare et al. 2006; Oehy and Schleiss 2007) can promote greater settling of sediment particles and thus induce turbidity currents to die out around the obstacles. They applied three-dimensional numerical models and laboratory experiments to investigate the effects of obstacles on the propagation of the turbidity currents of Lake Lugano. It is clear that bottom obstacles would be effective against bottom density currents but would fail against surface density currents. Understanding the physical processes and the type of density current then becomes essential to determine which type of structure may be effective.

Three different propagation types of turbid density currents in a reservoir are widely recognized: (1) overflows, or surface flows; (2) interflows (i.e., intrusive currents); and (3) underflows; or bottom currents. The type depends on the density difference between river inflows and the reservoir waters. Water temperature and sediment concentration contribute to the density of inflowing water. If the reservoir water is warm and clear, the turbid inflows usually plunge and then propagate as density currents along the bottom as underflows. Turbidity underflows were observed in Lake Mead in the United States (Howard 1953); Katsurazawa Reservoir in Japan (Chikita and Okumura 1990); and Luzzone Reservoir in Switzerland (De Cesare et al. 2001). In contrast, when the tributary inflows are warmer than the reservoir waters, clear inflows rise to the surface of the reservoir and propagate as overflows. On the other hand, when the receiving reservoir waters becomes thermally stratified, the turbid inflows may intrude near the thermocline as interflows, as sketched in Fig. 2 (Ford and Johnson 1983; Chen et al. 2006; Chung et al. 2009). The flow pattern of turbid density currents is also affected by variable thermal stratification, sediment concentration and particle size, and unsteady tributary inflows (Ford and Johnson 1983; Chung et al. 2009). In the case of sediment flushing near estuary barrages (Ji et al. 2011), salinity may become another factor in the determination of the density of surface waters.

[1]Manager, Korea Water Resources Corporation, Daejeon, South Korea; formerly, Postdoctoral, Dept. of Civil and Environmental Engineering, Colorado State Univ., Fort Collins, CO 80523.

[2]Professor, Dept. of Civil and Environmental Engineering, Colorado State Univ., Fort Collins, CO 80523 (corresponding author). E-mail: pierre@ engr.colostate.edu

Note. This manuscript was submitted on March 12, 2013; approved on December 4, 2013; published online on February 20, 2014. Discussion period open until July 20, 2014; separate discussions must be submitted for individual papers. This paper is part of the ***Journal of Hydraulic Engineering***, © ASCE, ISSN 0733-9429/05014004(15)/$25.00.

**Fig. 1.** Intrusion of highly turbid waters into Imha Reservoir during Typhoon Maemi in 2003 (reprinted with permission from the Korea water resources corporation)

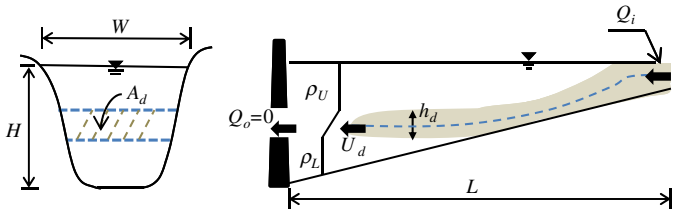


**Fig. 2.** Sketch of 1D continuity for a intrusive density current in a stratified reservoir

Numerical simulations can provide insight into time and spatially varied physical processes of density currents. One-dimensional (1D) numerical models need simpler boundary conditions and can be useful in the case of simple reservoir geometries without thermal stratification (Gosink 1987; Fang 2004; Balistrieri et al. 2006; Bell et al. 2006). Two-dimensional (2D) models are required to simulate narrow or shallow reservoirs and are indicated when averaging in either the lateral or vertical direction is possible. The lateral averaging 2D models are most often employed to examine the flow in stratified reservoirs (Cole and Wells 2006; Chung and Gu 1998; Williams 2007). Yi et al. (2005) applied a laterally averaged 2D model to Imha Reservoir during the summer stratification. They investigated the intrusion of turbid density currents caused by Typhoon Rusa in 2002. Imha Reservoir has experienced severe turbidity problems during Typhoon Maemi in 2003. Lee et al. (2007) simulated the propagation of turbid density currents in Imha Reservoir during Typhoon Ewiniar in 2006. They examined the efficiency of selective withdrawal facilities installed to reduce the increased persistent turbiditiy during the flood season.

To provide more physical insight into the hydrodynamic processes of a stratified reservoir, the application of three-dimensional (3D) models has recently attracted attention. The development and applications of several 3D hydrodynamic models for the simulation of density currents include the estuary, lake and coastal ocean model (ELCOM) (Hodges and Dallimore 2007), the unstructured tidal residual intertidal and mudflat model (UnTRIM) (Cheng and Casulli 2001), and the environmental fluid dynamics code (EFDC) (Hamrick 1992; Çalışkan and Elçi 2009).

The three-dimensional models typically solve the Reynolds-averaged Navier–Stokes (RANS) equations, mass conservation equations, free-surface equations, and the equation of state that relates to the fluid density, which depends on temperature and sediment concentration. To simplify the governing equations, the models generally use the Boussinesq, hydrostatic, and incompressible fluid assumptions. The hydrostatic assumption neglects vertical acceleration and nonhydrostatic pressure gradients, so it is generally employed for a reservoir in which horizontal length scales are larger than vertical scales (Hodges 2009). Çalışkan and Elçi (2009) applied the EFDC to investigate the effects of selective withdrawal of highly turbid waters on water quality. They found discrepancies between measured and simulated results and concluded that these were attributable to the hydrostatic assumption. Laval et al. (2003), and Wadzuk and Hodges (2004) suggested that nonhydrostatic pressure plays a crucial role in controlling internal wave evolution, which can influence mixing in a density stratified water body. Chen (2005) compared hydrostatic and nonhydrostatic pressure components in shallow water and found that the nonhydrostatic pressure gradient affects the velocity field and is not negligible even in the case of shallow waters. Weilbeer and Jankowski (2000) conducted a series of numerical experiments to investigate the hydrodynamical processes in the vicinity of structures using a 3D nonhydrostatic model. Fringer et al. (2006) presented the numerical results of lock-exchange gravity currents using the Stanford SUNTANS model and discussed the differences between hydrostatic and nonhydrostatic results. They showed that the hydrostatic simulation cannot correctly reproduce the formation of Kelvin–Helmholtz billows and the propagation speed of density currents. Turbulent mixing at the interface between the density current and ambient water is still an active fundamental research area (Venayagamoorthy and Stretch 2010).

The present study provides a detailed analysis of the dynamics of turbid density currents in Imha Reservoir, South Korea, using the 3D nonhydrostatic computational fluid dynamics (CFD) code FLOW-3D (2007). Simulations with other codes may be possible, but FLOW-3D allowed the authors to develop and couple a particle dynamics algorithm to simulate turbid density currents consisting of different particle sizes. The particle dynamics algorithm expands beyond the original FLOW-3D code in two ways: (1) it computes the changes in density through particle deposition; and (2) it includes multiple sediment sizes in mixtures of different particle sizes. This coupled code has been tested with laboratory experiments by An (2011) and An et al. (2012). The specific purpose of this study is to test the applicability of this approach to solve engineering problems at the prototype scale. The case study of Imha Reservoir has been selected because of the availability of field data to test the 3D model.

The main objectives of this study are (1) to test a new particle dynamics algorithm for the simulation of the density currents in Imha Reservoir during Typhoon Ewiniar; (2) to examine the range of sediment particle sizes for which density currents are possible; and (3) to determine the range of sediment concentrations for which interflows are possible during the summer months. Approximate analytical solutions for estimating propagation speed and intrusion depth of turbid density currents are also tested with the prototype measurements. To achieve the last two objectives, the calibrated 3D model is subjected to a parametric analysis for different inflow characteristics (i.e., sediment particle size, sediment concentration) and seasonal changes in thermal stratification of the reservoir. This approach will assist field engineers to estimate the type, propagation speed, and intrusion height of turbid density currents in a stratified reservoir as a function of thermal stratification profiles, incoming sediment concentration, and particle size distribution.

## Imha Reservoir and Turbidity Problems

Imha Reservoir is located (36°32′N; 128°53′E) in the northeastern part of the Nakdong River basin in South Korea. It is the major water source for the northern Gyeongbuk province. Its annual water supply capacity is approximately $497 \times 10^6$ m$^3$ and has a flood control capacity of $80 \times 10^6$ m$^3$. It also contributes to the annual power generation of 96.7 GW · h. The watershed area of Imha Reservoir covers 1,361 km$^2$, drained by three major tributaries: Ban-byun Stream; Yong-jun Stream; and Dae-gok Stream. The mean annual rainfall measured ranged from 1,029 to 1,248 mm at three stations located near Imha Reservoir, based on hydrological observations over the past 20 years. The reservoir is relatively long and narrow with a riverbed slope of 0.11% and a width that ranges from 300 to 1,000 m. The maximum water depth is about 60 m near the dam site.

Kim and Julien (2006) estimated the annual average soil loss at approximately 3,450 t/km$^2$. Typically, the largest soil loss occurs during severe rainfall events such as typhoons. One of the main reasons for the high soil loss rate in the Imha watershed is that the watershed has a weak resistance to soil erosion as a result of geology and land cover conditions (Lee and Cho 2004). The large soil losses during severe floods trigger the intrusion of highly turbid waters into Imha Reservoir. During the summer months since 2002, Imha Reservoir has frequently experienced turbid density currents propagating along the thermocline. The highest turbidity values were recorded during Typhoons Rusa in 2002 and Maemi in 2003 with 880 and 1,200 NTU, respectively. Moreover, successive turbidity inflows during large runoff events have resulted in persistently elevated turbidity levels. The addition of flocculants has been required to comply with the limitating regulation of 5 NTU for water treatment.

Typhoon Ewiniar on July 10, 2006, has been selected for this study because of the availability of field measurements for testing the numerical model. During Typhoon Ewiniar, the total inflow volume entering the reservoir roughly reached $100 \times 10^6$ m$^3$, which was equal to 25% of the effective capacity of the reservoir ($424 \times 10^6$ m$^3$). Because of the large inflow volume within a relatively short period of time (35 h), typhoons obviously control the reservoir dynamics. Inflow mixing is a dominant factor to account for the dynamics of turbid density currents.

### *Field Measurements*

Real-time gauging stations were installed by Korea Water Resources Corporation (K-water) at five different stations to monitor the turbid density currents propagating from each of the tributaries into the reservoir. The monitoring devices work with a data logging system to store the collected data of temperature and turbidity (NTU), pH, conductivity, and dissolved oxygen (DO) at every 1.0-m depth interval. Turbidity sensors (Troll 9000) can measure up to 2,000 NTU and provide a resolution of 0.1 NTU. The data acquisition process is also compatible with real-time data logging systems. The data are transmitted in real time at intervals of 1 or 2 h from the gauging stations to the Dam Integration Information System (DIIS) of K-water using the Mugunghwa satellite. Fig. 3 shows a time series of peak turbidity and other relevant parameters such as precipitation, wind speed, and wind direction, which are also available from the DIIS during Typhoon Ewiniar. The time series of depth-averaged turbidity are used as input parameters to the numerical model. Peak turbidities were 2,400, 2,600, 850, and 800 NTU at the stations and decreased in the downstream direction.

Imha Reservoir shows a stable thermal stratification in the early summer. Fig. 4 shows a series of vertical temperature profiles in 2006 near Imha Dam. As the increased heating and wind-driven mixing occur during the summer months, the epilimnion develops approximately $5 \sim 10$ m deep below the free surface. Strong thermal stratification is observed during the typhoon season from July to September. The maximum temperature gradient is found $10 \sim 20$ m below the free surface during the summer months.

The particle size distributions in the turbid density currents, sampled during floods in 2005 and 2011, are shown in Fig. 5. The sediments of the inflowing streams contain widely ranged particles varying from clay to sand (1 to 100 $\mu$m) with the median particle size $d_s \cong 20$ $\mu$m. In the reservoir, the particle size distributions show finer sediments than the inflowing streams, and the median particle size $d_s$ ranges from 2 to 10 $\mu$m. This suggests that the large sediment sizes cannot be carried in suspension by the intrusive density currents that reach Imha Dam. A particle size of 5 $\mu$m was used as representative of the sediments within the turbidity currents of the entire reservoir.

To simulate the turbid density currents, the conversion between the suspended sediments (SS) (mg/L) and turbidity (NTU) is required. The SS-NTU relationship has been determined from laboratory measurements using field data of turbidity and concentration. K-water (2007) obtained the ratio SS/NTU = 0.7 in the reservoir and SS/NTU = 0.5 in the river inflow (An 2011).

## Plunge Depth and Propagation Speed

An analytical solution is presented to approximately calculate the propagation speed of turbid density currents in stratified reservoirs. The derivation assumes that the inflow discharge and reservoir width are constant. The governing equations include the continuity equation and a celerity relationship described only in terms of the density current height and density difference between the riverine inflow and the reservoir waters. The one-dimensional continuity equation defining the conservation of fluid mass in the density current without lateral inflow is given by

$$\frac{\partial Q_i}{\partial x} + \frac{\partial A_d}{\partial t} = 0 \tag{1}$$

where $Q_i$ = inflow discharge of the density current; and $A_d$ = cross-sectional area of the density current. When considering a one-dimensional reservoir (Fig. 2) with a constant width, Eq. (1) can be written as

$$\frac{Q_i - Q_o}{L} = W\frac{dH}{dt} \tag{2}$$

where $Q_o$ = outflow discharge at the dam; $W$ = reservoir width; $L$ = reservoir length; and $dH/dt$ = rate of change in the water surface elevation of a reservoir during a flood. When $Q_o = 0$, Eq. (2) reduces further to

$$Q_i = Wh_dU_d = LW\frac{dH}{dt} \tag{3}$$

where $h_d$ = intrusive depth of a density current, where the gradual increase of $h_d$ resulting from interfacial water entrainment is assumed to be small; and $U_d$ = depth-averaged propagation speed, or celerity of a density current. After dividing by $W$, the 1D continuity equation simply reduces to

$$U_d = \frac{L}{h_d}\frac{dH}{dt} \tag{4}$$

which shows that the celerity is inversely proportional to the density current thickness.

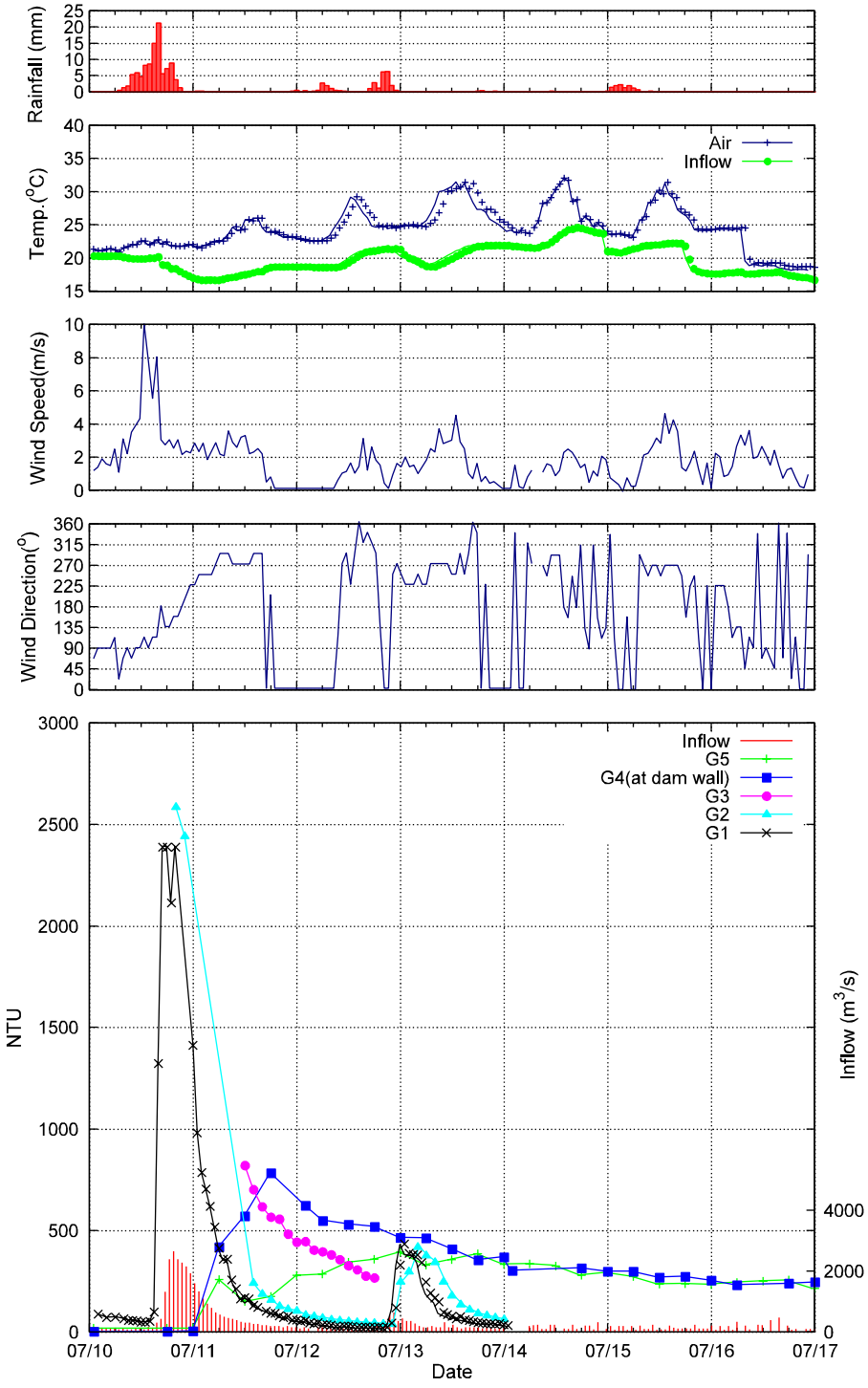


**Fig. 3.** Monitored data during Typhoon Ewiniar in July 2006; features of the flood event include hydrologic data and a time series of maximum vertical turbidity measurements at each station

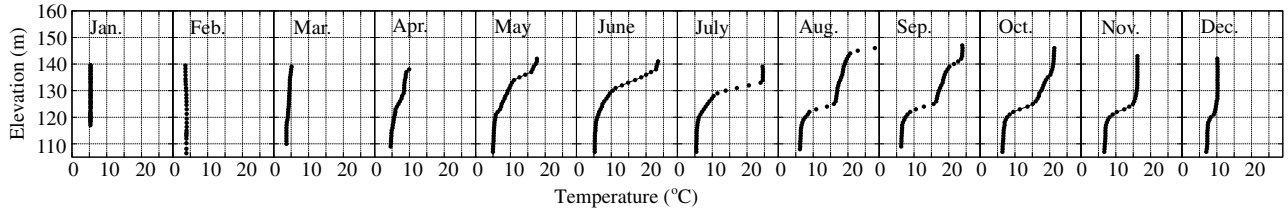


**Fig. 4.** Seasonal variations in water temperature measured at the Imha Reservoir (G2) in 2006

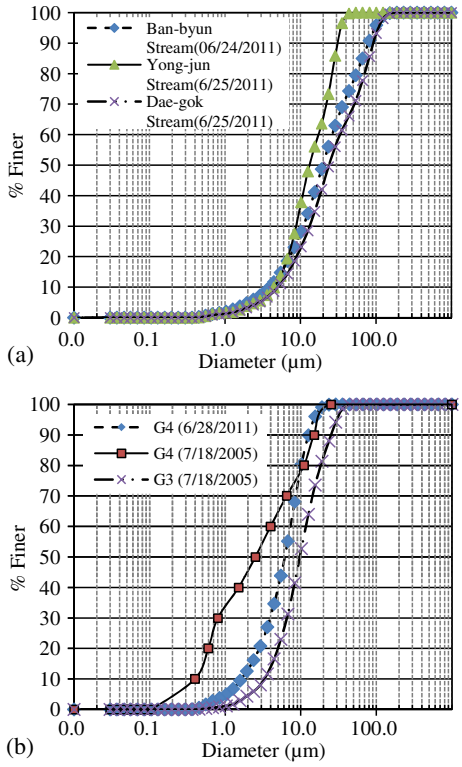


**Fig. 5.** Particle size distributions of sediments in the turbid density currents, measured at different locations in the reservoir and in the tributaries, respectively

The depth-averaged propagation speed $U_d$ of a density current can be described in terms of depth and density difference, defined in general form as

$$U_d = C\sqrt{g'h_d} \tag{5}$$

where $C$ = coefficient; and $g'$ = reduced gravity, which is given by $g' = g(\Delta\rho/\rho_r)$, where $\Delta\rho$ denotes the density difference between ambient fluid and a density current, and $\rho_r$ indicates a reference density. From laboratory experiments of bottom density currents. Keulegan (1957) found $C = 0.76$, and Middleton (1966) found $C = 0.75$.

In the case of intrusive density currents (sketched in Fig. 2), Benjamin (1968) applied the inviscid-fluid theory at values of $h_d/H$ increasing from 0.0 to 0.5. He obtained the formula for the depth-averaged celerity of a density current as a function of the fractional depth ($h_d/H$):

$$C = \frac{U_d}{\sqrt{g'h_d}} = \frac{1}{\sqrt{2}}\left[\frac{(H-h_d)(2H-h_d)}{H(H+h_d)}\right]^{1/2} \tag{6}$$

where $g' = 0.5g(\rho_U - \rho_L)/\rho_L$; and $\rho_U$ and $\rho_L$ = mass density of the upper and lower fluid layer, respectively.

Kao (1977) derived the celerity of a density current of mass density $\rho_d$ along a sharp interface between two homogeneous fluids on the basis of the Bernoulli theorem and obtained

$$U_d = \sqrt{2\frac{\rho_L - \rho_d}{\rho_d}\frac{\rho_d - \rho_U}{\rho_L - \rho_U}gh_d} \tag{7}$$

where in Eq. (7) $g' = [(\rho_L - \rho_d)/\rho_d][(\rho_d - \rho_U)/(\rho_L - \rho_U)]g$ and $C = \sqrt{2}$.

Substituting Eq. (5) into Eq. (4) yields a relationship for the intrusive depth:

$$h_d = \left[\frac{L^2}{g'}\left(\frac{dH}{dt}\right)^2\frac{1}{C^2}\right]^{1/3} \tag{8a}$$

which, from Eq. (3) can also be rewritten as

$$h_d = \left[\frac{L^2}{g'}\left(\frac{Q_i}{A_s}\right)^2\frac{1}{C^2}\right]^{1/3} \tag{8b}$$

where $A_s$ = surface area of the reservoir. Eqs. (5) and (8) can be used to predict the propagation speed and intrusion depth of turbid density currents.

## Numerical Model Description

In this study, FLOW-3D was selected because it exploits the highly accurate and improved volume of fluid (VOF) technique (Hirt and Nichols 1981), which can provide an accurate simulation of density flows in a layer stratified environment. Density currents are powered by the density difference, which determines how far the density currents propagate.

### *Governing Equations*

The governing equations solved with FLOW-3D are very briefly described here: (1) the 3D Reynolds-Averaged Navier-Stokes (RANS) equations for fluid flow with the Boussinesq approximation; (2) the continuity equation; and (3) the transport equations for each scalar variable. A scalar equation is used to compute advection, diffusion, and dispersion of scalars (e.g., sediment and temperature). These equations are given in tensor notation by

$$\frac{\partial u_i}{\partial t} + u_j\frac{\partial u_i}{\partial x_j} = -\frac{1}{\rho_r}\frac{\partial p}{\partial x_i} + \frac{\partial}{\partial x_j}\left(\nu\frac{\partial u_i}{\partial x_j} - \overline{u_i'u_j'}\right) + g_i\frac{\rho-\rho_r}{\rho_r} \tag{9}$$

$$\frac{\partial u_i}{\partial x_i} = 0 \tag{10}$$

$$\frac{\partial \varphi}{\partial t} + \frac{\partial}{\partial x_i}(u_i\varphi) = \frac{\partial}{\partial x_i}\left(\Gamma\frac{\partial \varphi}{\partial x_i} - \overline{u_i'\varphi'}\right) \tag{11}$$

where $u_i$ = the mean velocity components in a Cartesian coordinate system ($x$, $y$, $z$); $t$ = time; $\rho_r$ = reference density; $p$ = total pressure; $\nu$ = fluid kinematic viscosity; $-\overline{u_i'u_j'}$ = Reynolds stresses; $g_i$ = gravitational acceleration components in each direction; $\Gamma$ = molecular diffusivity of the scalar $\varphi$; $-\overline{u_i'\varphi'}$ = turbulent fluxes of the scalar $\varphi$; and $\rho$ = density, which can be calculated as a function of temperature and sediment concentration. The overbar (-) denotes averaging of fluctuating quantities. Eq. (11) solves scalar transport and it is coupled with Eq. (9) only through the buoyancy term with the Boussinesq approximation.

The Reynolds stresses ($\overline{u_i'u_j'}$) can be generally modeled using the turbulent viscosity hypothesis (Pope 2000):

$$-\overline{u_i'u_j'} = \nu_t\left(\frac{\partial u_i}{\partial x_j} + \frac{\partial u_j}{\partial x_i}\right) - \frac{2}{3}k\delta_{ij} \tag{12}$$

where $\nu_t$ = turbulent (eddy) viscosity; $\delta_{ij}$ = Kronecker delta; and $k$ = turbulent kinetic energy. In Eq. (11), the $-\overline{u_i'\varphi'}$ term represents the turbulent scalar flux and is given by

$$-\overline{u_i'\varphi'} = \Gamma_t\frac{\partial \varphi}{\partial x_i} \tag{13}$$

where $\Gamma_t$ = turbulent scalar diffusivity defined as $\Gamma_t = \nu_t/Sc_t$ in which $Sc_t$ is the turbulent Schmidt number and is generally obtained from laboratory experiments. A turbulent Schmidt number $Sc_t = 5$ was found to be suitable for intrusive turbidity currents based on the model calibration with laboratory measurements (An 2011).

In this study, the renormalization-group (RNG) $k-\varepsilon$ closure scheme was employed. In the RNG $k-\varepsilon$ model, the eddy viscosity is defined as

$$\nu_t = c_\mu k^2/\varepsilon \tag{14}$$

where $c_\mu$ = empirical constant; and $\varepsilon$ = turbulence kinetic energy dissipation rate. In Eq. (14), the turbulence kinetic energy ($k$) and its dissipation rate ($\varepsilon$) are obtained from the following transport equations:

$$\frac{\partial k}{\partial t} + u_j \frac{\partial k}{\partial x_j} = \frac{\partial}{\partial x_j}\left(\frac{\nu_t}{\sigma_k}\frac{\partial k}{\partial x_j}\right) + P + G - \varepsilon \tag{15}$$

$$\frac{\partial \varepsilon}{\partial t} + u_j \frac{\partial \varepsilon}{\partial x_j} = \frac{\partial}{\partial x_j}\left(\frac{\nu_t}{\sigma_\varepsilon}\frac{\partial \varepsilon}{\partial x_j}\right) + c_{1\varepsilon}\frac{\varepsilon}{k}(P + c_{3\varepsilon}G) - c_{2\varepsilon}\frac{\varepsilon^2}{k} \tag{16}$$

where $P$ and $G$ are defined as

$$P = \nu_t\left(\frac{\partial u_i}{\partial x_j} + \frac{\partial u_j}{\partial x_i}\right)\frac{\partial u_i}{\partial x_j} \tag{17}$$

$$G = g_i \frac{\nu_t}{Sc_t}\frac{1}{\rho_r}\frac{\partial \rho}{\partial x_i} \tag{18}$$

There are five parameters in Eqs. (14)–(16) derived explicitly in the RNG model. In this study, the parameter values obtained from the literature (Yakhot et al. 1992) are used: $c_\mu = 0.085$; $c_{1\varepsilon} = 1.42$; $c_{3\varepsilon} = 0.2$; $\sigma_k = 1.39$; and $\sigma_\varepsilon = 1.39$. In the RNG model, $c_{2\varepsilon}$ is a function of the shear rate, computed from the equation that is given by

$$c_{2\varepsilon} = 1.83 + \frac{c_\mu \eta^3(1-\eta/\eta_o)}{1+\beta\eta^3} \tag{19}$$

where $\eta_o = 4.38$; and $\beta = 0.015$. The parameter $\eta = Sk/\varepsilon$ and $S = \sqrt{2S_{ij}S_{ij}}$ where $S_{ij}$ represents the strain rate tensor given by

$$S_{ij} = \frac{1}{2}\left(\frac{\partial u_i}{\partial x_j} + \frac{\partial u_j}{\partial x_i}\right) \tag{20}$$

An et al. (2012) provided a thorough parameter calibration and a verification with detailed laboratory measurements before the numerical model could be used for this field scale application. This demonstrated that numerical simulations with parameter values obtained from the literature (Yakhot et al. 1992) compare very well with laboratory experiments (Sutherland et al. 2004).

### Particle Dynamics Algorithm

A new particle dynamics algorithm has been developed and coupled with the CFD model for the simulation of density currents with particle settling in reservoirs. The new particle dynamics algorithm describes the motion by particle-driven buoyant forces attributable to sediment concentration and settling. The settling velocities $\omega_s$ are computed according to Stokes' law, defined as

$$\omega_s = \frac{g d_s^2}{18\nu}\left[\frac{\rho_s - \rho_w(T)}{\rho_w(T)}\right] \tag{21}$$

where $\rho_w(T)$ = water density defined as a function of temperature from Gill (1982). The temporal evolution of the sediment particle field can then be treated in an Eulerian manner in a turbulent advection-dffusion Eq. (11) and the result is

$$\frac{\partial \varphi}{\partial t} + \frac{\partial}{\partial x_i}(u_i\varphi) = \frac{\partial}{\partial x_i}\left(\Gamma\frac{\partial \varphi}{\partial x_i} - \overline{u_i'\varphi'}\right) + \frac{\partial}{\partial z}(\omega_s\varphi) \tag{22}$$

where the last term describes particle settling.

In the computational cell ($i$, $j$, $k$), the fluid mass density $\rho_{ijk}^n$ at time level $n$ is computed as a function of temperature and particle concentration as follows:

$$\rho_{ijk}^n = \rho_w(T)_{ijk}^n\left[1 + (G-1)\frac{V_{s_{ijk}}^n}{V_{ijk}^n}\right] \tag{23}$$

where $\rho_w(T)_{ijk}^n$ = water density in a cell at temperature $T$ in °C; $V_{s_{ijk}}^n$ = volume of solid particles in the cell ($i$, $j$, $k$), which is updated each time step because of particle settling algorithm illustrated in Fig. 6; $V_{ijk}^n$ = total fluid volume in the cell ($i$, $j$, $k$); and $G$ = constant specific gravity of sediment particles.

The particle dynamics algorithm has been tested with the laboratory experiments of Gladstone et al. (1998) by An et al. (2012). Once the model has been validated, different particle sizes could then be simulated to determine what particle sizes settle out of sediment laden density currents.

### Numerical Solution

The main attributes of FLOW-3D are very briefly reviewed here. The numerical model solves the governing equations using finite-difference approximations. Each cell is associated with local average values of all dependent variables. All dependent variables are located at the cell center except for velocities, which are located at cell faces (staggered grid arrangement). Most terms in the equations are evaluated explicitly, which produces a simple and efficient computational scheme. The finite-difference approximation of Eq. (9) is defined as

$$u_{i,j,k}^{n+1} = u_{i,j,k}^n + \delta t^{n+1}\left(-\frac{p_{i+1,j,k}^{n+1} - p_{i,j,k}^{n+1}}{(\rho\delta x)_{i+1/2,j,k}^n} + T_x\right) \tag{24}$$

$$v_{i,j,k}^{n+1} = v_{i,j,k}^n + \delta t^{n+1}\left(-\frac{p_{i,j+1,k}^{n+1} - p_{i,j,k}^{n+1}}{(\rho\delta y)_{i,j+1/2,k}^n} + T_y\right) \tag{25}$$

$$w_{i,j,k}^{n+1} = w_{i,j,k}^n + \delta t^{n+1}\left(-\frac{p_{i,j,k+1}^{n+1} - p_{i,j,k}^{n+1}}{(\rho\delta z)_{i,j,k+1/2}^n} + T_z\right) \tag{26}$$

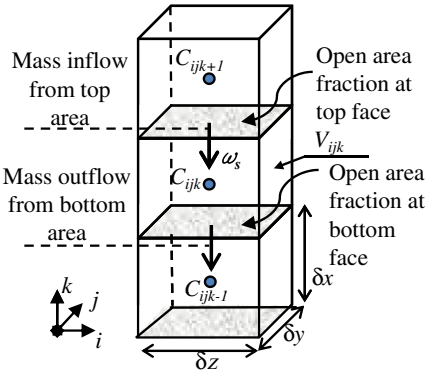


**Fig. 6.** Schematic of particle settling and concentration change $C_{ijk}$ in cell ($i$, $j$, $k$)

where $i$, $j$, $k$ = indices of cell in the cell for a Cartesian grid system ($x$, $y$, $z$ coordinates); and $T$ indicates all terms involving the advective, viscous, and gravitational acceleration meaning. In the term $T$, the spatial gradient terms such as advective fluxes $u\partial u/\partial x$ tend to decrease numerical accuracy with employing variable meshes for the spatial discretization. Therefore, the numerical model developed is a modified donor-cell approximation that can retain its accuracy in nonuniform meshes (FLOW-3D 2007). The finite-difference approximation in the modified donor-cell approximation, the $u\partial u/\partial x$, is defined as

$$(u_r - \alpha u_r)\frac{(u_{i+1,j,k} - u_{i,j,k})}{\delta x_{i+1}} + (u_l + \alpha u_l)\frac{(u_{i,j,k} - u_{i-1,j,k})}{\delta x_i} \quad (27)$$

where $u_r = 0.5(u_{i+1,j,k} + u_{i,j,k})$; and $u_l = 0.5(u_{i,j,k} + u_{i-1,j,k})$. When $\alpha = 0$, this scheme reduces to a second-order, centered-difference approximation; and when $\alpha = 1$, the first-order, donor-cell approximation is recovered. The basic concepts of this scheme is to weight the upstream quantity being fluxed more than the downstream value using factors $(1 + \alpha)$ and $(1 - \alpha)$ for each direction, respectively. In this study, first-order approximation scheme is used for all advective flux terms appearing in Eqs. (24)–(26) to efficiently simulate a large field domain.

The model adjusts a time-step size so that the fluid does not flow across more than one cell in one computational time step, $\delta t$, which is refered to as a courant stability criterion, defined as

$$\delta t < 0.45 \cdot \min\left(\frac{V_f \delta x_i}{A_x u}, \frac{V_f \delta y_j}{A_y v}, \frac{V_f \delta z_k}{A_z w}\right) \quad (28)$$

where $V_f$ and $A$ = fractional volume and area, open to flow in the fractional-area-volume-obstacle-representation method. In FLOW-3D, if the automatic time-step is selected, the model adjusts the time step to be as large as possible while keeping the stability criteria.

## Density Current Modeling at Imha Reservoir

### Computational Grid

The bathymetric survey of Imha Reservoir by K-water (2007) provides topographic and bathymetric data for the production of a digital elevation model (DEM). The DEM was created using a geographic information system (GIS) tool that can incorporate the bathymetric survey data into topographic data. The sophisticated methods for defining complex geometric regions (e.g., bathymetry, the surface terrain, and hydraulic structures) into the grid systems of the numerical model are needed for the simulation of the density currents passing the complex geometries. AutoCAD and Arcview GIS software were used to create the 3D bathymetric model as a high-resolution stereolithography (STL) format, which can be exported to the FLOW-3D model. The authors employed a relatively high-resolution discretization grid. The vertical layers below the water surface were represented by 1-m depth increment ($\Delta z = 1.0$ m) throughout the reservoir water column, whereas horizontal grid sizes were chosen to be 25.0 m ($\Delta x, \Delta y = 25$ m) with a total of 2.5 million cells.

The numerical simulations were performed on two personal computers with the hardware platforms of 3.2 GHz Quad-Core (i7), 4GB memory. The overall dynamics of turbid density currents entering Imha Reservoir during the flood were accurately replicated. The three-dimensional simulations of density currents, however, are computationally very expensive. Thus, the shared-memory parallel version of FLOW-3D code was employed, available on a multicore computer, allowing for efficient parallelism.

### Initial and Boundary Conditions

Boundary conditions should be imposed at the bottom and sides of a reservoir for which the wall boundary is specified as a nontangential stress area with a no-slip condition for which the roughness height was set to 0.01 m. A logarithmic law of wall function (Rodi 1980) is used to compute $k$ and $\varepsilon$ at the wall. We set $k = u_*^2\sqrt{C_\mu}$ and $\varepsilon = u_*^3/\kappa y_o$ where $u_*$ = shear velocity; $\kappa$ = von Kármán constant (0.41 used in this model); $y_o$ = normal distance from the boundary wall to the location of tangential velocity. The free surface was specified as a slip boundary (i.e., zero shear stress).

The simulation setup for this study is based on field data observed during Typhoon Ewiniar (Fig. 3). The inlet boudary was specified with velocity, temperature, and sediment concentration. Velocity at the inlet boundary was calculated from the inflow measurements. Water temperature and suspended sediment concentration profiles at the reservoir inlet were also included for the boundary setup and model calibration requirements using the field measurements. At each simulation time step, all field data should be linearly interpolated to specify the inlet boundary condition. The average median grain size $d_{50} \cong 5$ $\mu$m that was measured in the reservoir was employed for the simulations.

The time series of field data for water temperature and turbidity profiles at Buoy-point (near the dam wall) were also used to set the initial conditions and compared with numerical results. The simulated outflow boundary was specified at a constant discharge (100 $m^3/s$) at the intake structure, which is very small compared to the inflow rates at the reservoir inlet during Ewiniar. It took approximately a week of clock time to perform a numerical simulation lasting 3 days (July 10–13, 2006).

### Model Calibration and Validation

The model calibration was done by replicating the downstream sediment concentrations and temperature measurements with validation of several intermediate profiles. Computed time-series plots illustrate the temporal variations of suspended sediments and are compared in Fig. 7 with the field measurements at three locations (G3, G4, and G5). The inflows showed fast propagation speeds in the transitional region (G2 ~ G3) because of the bed slope and narrow cross section, whereas the inflows reduced their propagation speed because they intruded horizontally into the lacustrine region (G3 ~ G5) in which its width is greater than that of the other regions (i.e., riverine or transitional region). Both the field measurements and simulation results indicate that the travel time of peak turbidity was 15 h from G3 to G4 and 30 h from G4 to G5.

The accuracy of the model to predict the vertical distribution of turbidity at several location in the reservoir has also been tested. The model has been accurately validated with hourly field measurements at three different gauging stations. The simulated and measured vertical profiles of turbidity and temperature at G4 are shown in Figs. 8 and 9, respectively. The results were equally good at stations G3 and G5 as reported by An (2011). The peak turbidity measurements were observed at approximately elavation 135.0 m and the intrusion depths ranged from 15 to 20 m. The numerical model provided very good predictions of the temporal evolution of temperature and turbidity induced by the intrusion of density currents.

### Model Performance

To quantitatively evaluate the model performance, the authors used the absolute mean error (AME) and the root mean square error (RMSE) defined by

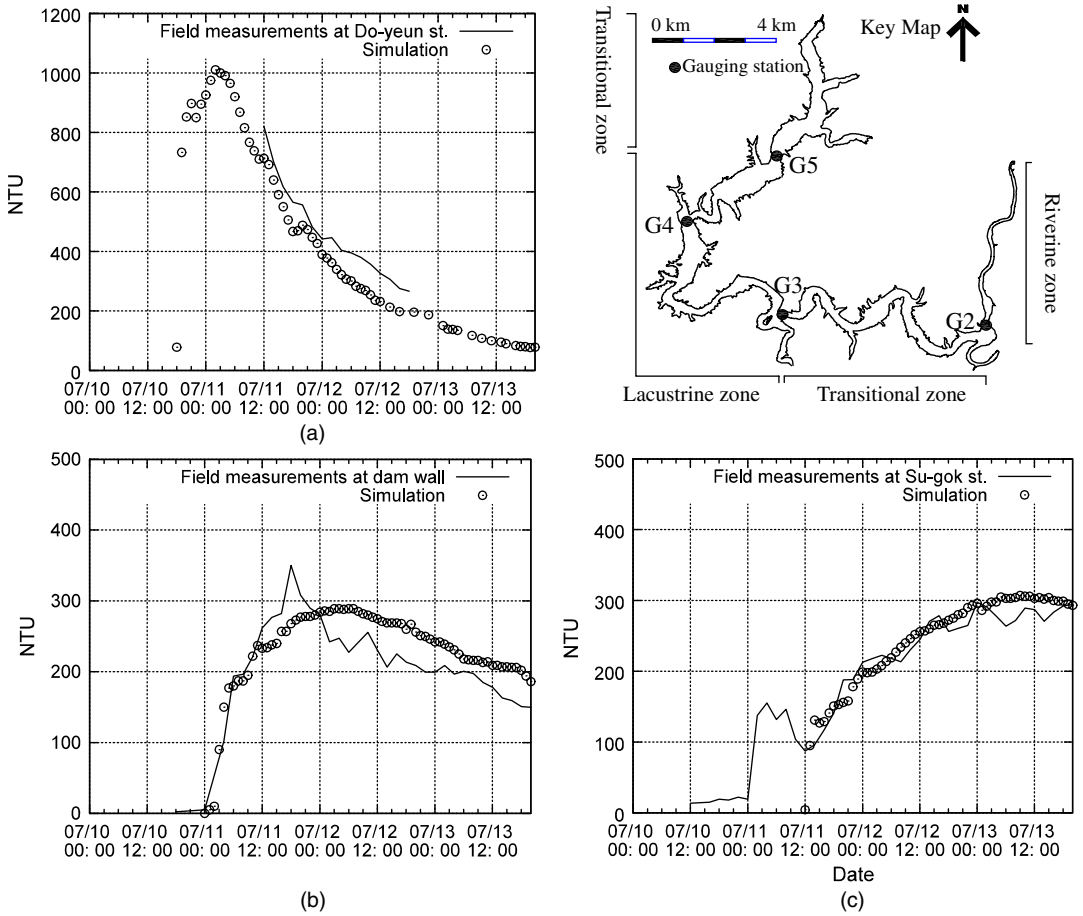


**Fig. 7.** Time-series plots of turbidity (NTU) for: (a) internal validation with field measurements at G3; (b) internal validation with field measurements at G4; (c) model calibration (G5)

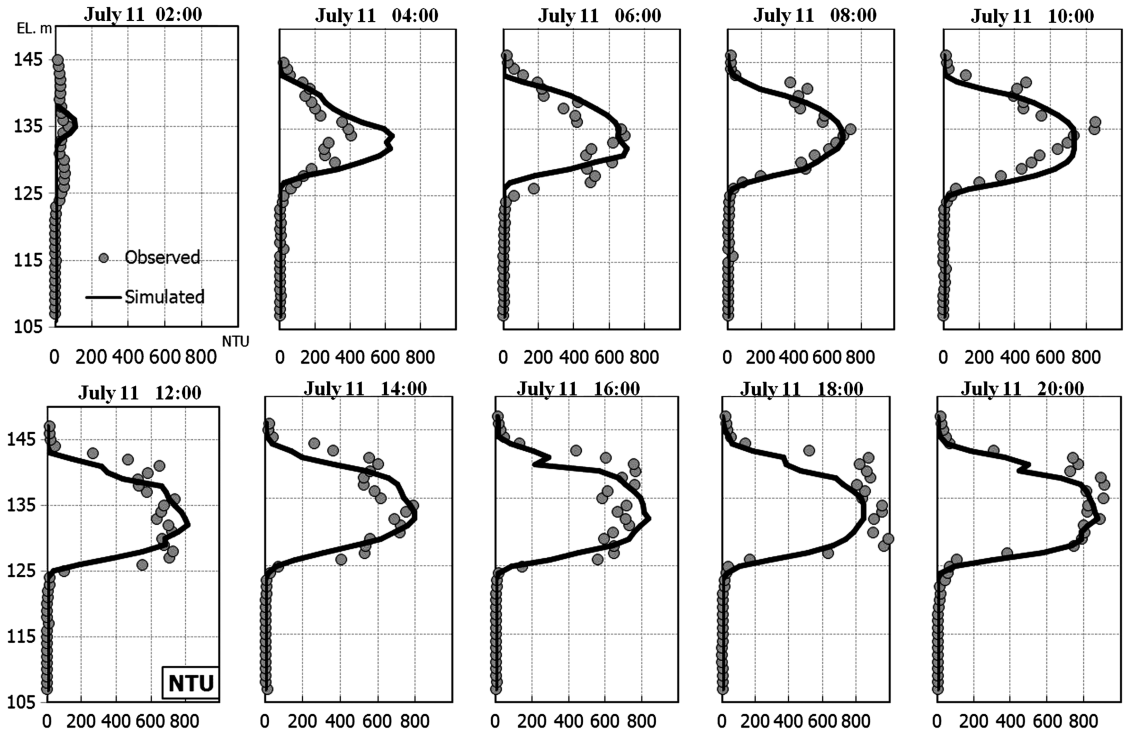


**Fig. 8.** Validation of vertical turbidity (NTU) profiles between the numerical model (lines) and field measurements (circles) at G4

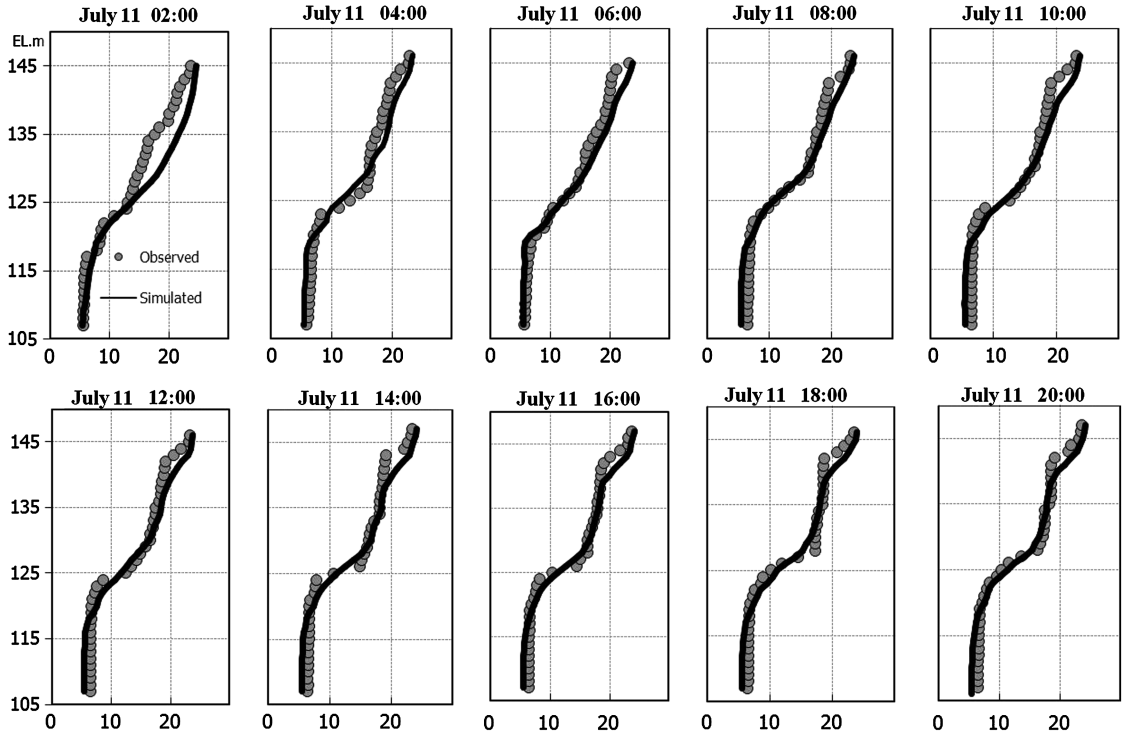


**Fig. 9.** Validation of vertical water temperature profiles between the numerical model (lines) and field measurements (circles) at G4

$$\text{AME} = \frac{1}{N_{\max}}\left(\sum_{N=1}^{N_{\max}} |M_N - S_N|\right) \tag{29}$$

$$\text{RMSE} = \sqrt{\frac{1}{N_{\max}}\sum_{N=1}^{N_{\max}} (M_N - S_N)^2} \tag{30}$$

where $N_{\max}$ = the number of data; $M_N$ = field measurements; and $S_N$ = simulation results.

As shown in Fig. 10, average AME and RMSE for temporal turbidity variations were 37.0 and 47.0 NTU, respectively, provided by comparing with the time series data of NTU measured at G3, G4, and G5 (time series of turbidity data). Values of AME and RMSE for water temperature profiles were 1.0 ℃ and 1.3 ℃ over a range of 5.0 ~ 24.0℃, respectively.

### *Intrusive Depth and Propagation Speed*

The propagation dynamics of interflow density currents can be described through maps of sediment concentration at different times. Figs. 11 and 12 show simulation results of sediment concentration at EL 141.0 m (10.0 m above thermocline) and near the thermocline (viewpoint at EL 131.0 m), respectively. These figures illustrate the temporal and spatial evolution of the intrusive density currents, as well as lateral mixing and longitudinal dispersion in the meandering reservoir during the flood.

The propagation speed can be calculated by dividing the length of the reservoir by peak travel time from G2 to G4. Table 1 shows a comparison of the analytical solutions with the reach average conditions between G2 and G4. They produce very similar predictions for the propagation speed and the intrusive depth of turbid density currents in Imha Reservoir. In this case, the propagation speed was approximately 0.2 m/s, which

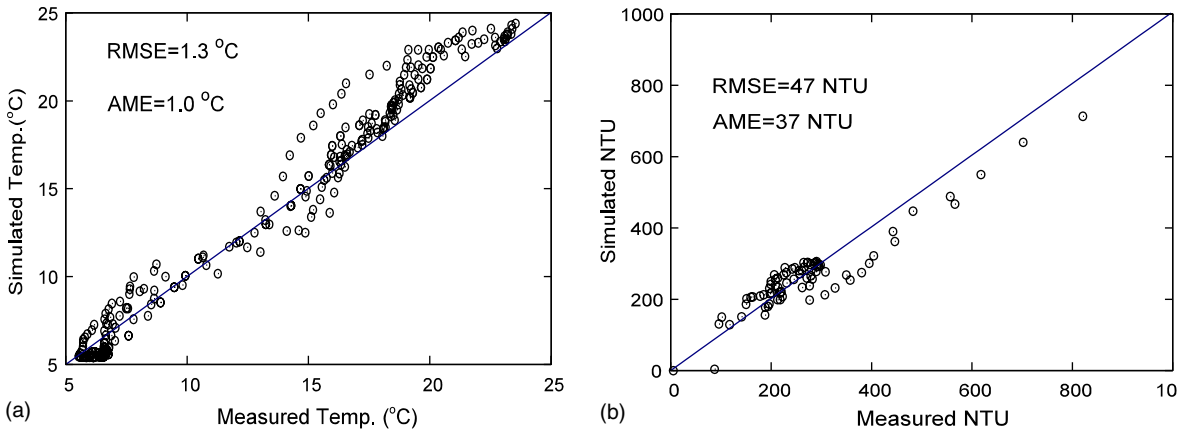


**Fig. 10.** Quantitative validation of: (a) temperature; (b) turbidity errors using AME and RMSE





J. Hydraul. Eng.

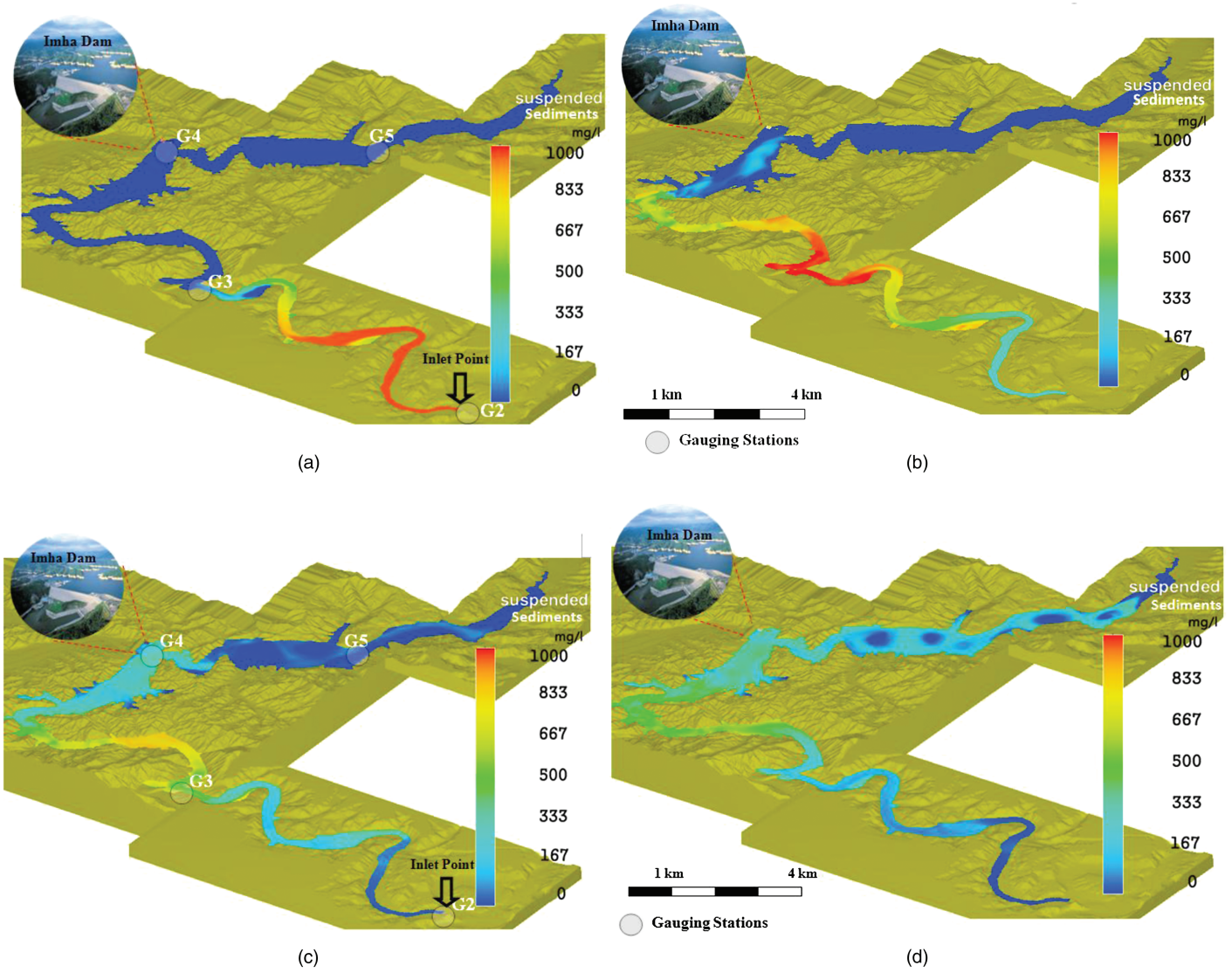


**Fig. 11.** (Color) Temporal and spatial distributions of suspended sediment concentration in mg/L at EL 141.0 m (10 m above thermocline) (reprinted with permission from the Korea Water Resources Corporation): (a) July 10, 1800 hrs.; (b) July 11, 0400 hrs.; (c) July 12, 0000 hrs.; (d) July 12, 1600 hrs.

corresponds to 17.3 km/day. The analytical solutions to the continuity equation and momentum equations yielded approximate solutions given by Eqs. (8) and (5) for the intrusive depth $h_d$ and the propagation speed $U_d$ of density currents, respectively.

### Plunge Depth

Most of the formulas using simplified steady-state analytical approach predict the plunge location by calculating plunge depth, which can be expressed as a general form:

$$h_p = \left(\frac{1}{\mathsf{F}_p^2}\right)^{1/3} \left(\frac{q_o^2}{g'}\right)^{1/3} \tag{31}$$

where $h_p$ = hydraulic depth at the plunge point; $\mathsf{F}_p$ = densimetric Froude number at the plunge point; $q_o$ = unit discharge for rectangular channel; and $g' = g(\rho_d - \rho_a)/\rho_a$ in which $\rho_a$ is the ambient surface density. Savage and Brimberg (1975) considered the effects of ratio of interfacial to bed friction $f_i/f_b$, bed friction, and bed slope $S_o$ on the plunge depth. For a rectangular cross section with constant width, the $\mathsf{F}_p$ are obtained from equations:

$$F_p \approx \frac{2.05}{1 + (f_i/f_b)} \left(\frac{S_o}{f_b}\right)^{0.478} \tag{32}$$

where $f_i = 0.004$ and $f_b = 0.02$ (Ford and Johnson 1983); and $S_o = 0.0011$, which was estimated from the reservoir bathymetry. The results calculated by Eqs. (31) and (32) and from the numerical simulations during the flood event are shown in Table 2.

The numerical simulations capture the dynamic chacteristics of plunge location rather well in Fig. 13. These transects illustrate the temporal and spatial evolution of the turbid density currents changing from plunging flows to interflows. The turbidity density currents plunged approximately 5 to 10 km from the dam at a corresponding plunge depth of $h_p = 20$–25 m during the typhoon event. The plunge location moves closer to the dam as inflows increase and moves back several kilometers upstream as inflows decrease.

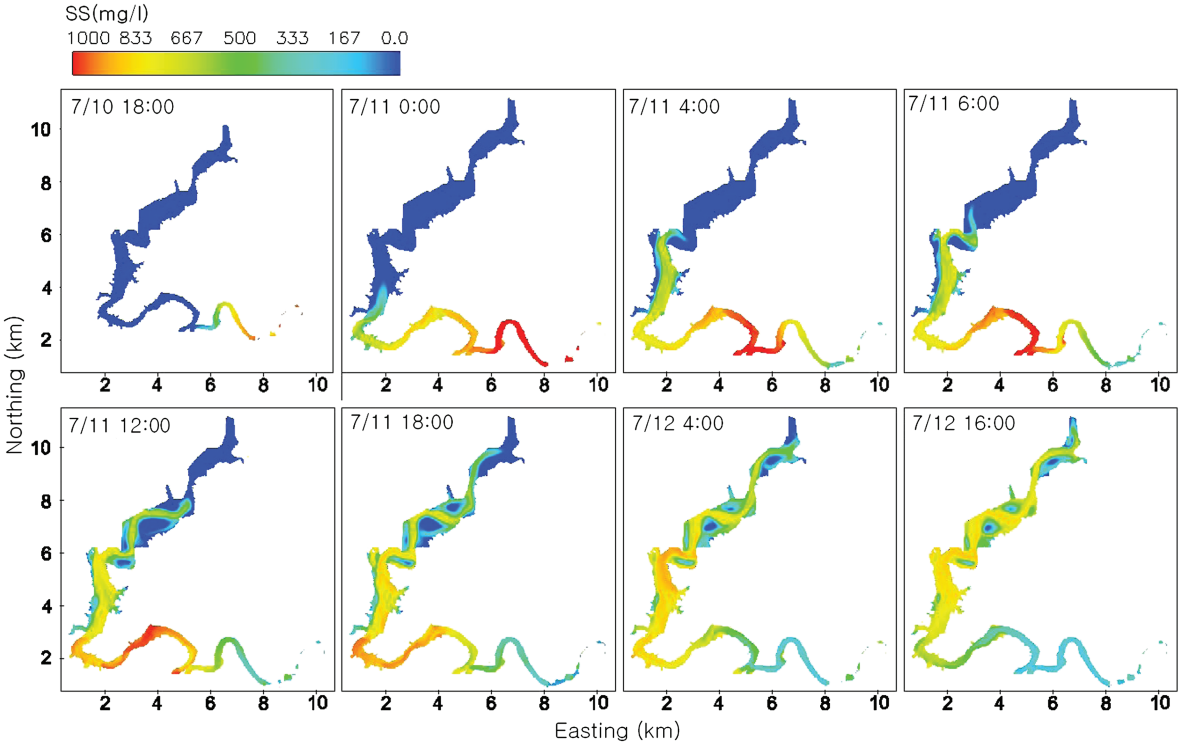


**Fig. 12.** (Color) Temporal and spatial distributions of suspended sediment in mg/L at EL 131.0 m (thermocline)

**Table 1.** Propagation Speed and Intrusion Depth of Turbid Density Currents Traveling from G2 to G4

| Method | $C$ | Propagation speed $U_d$ (m/s) | Intrusion depth $h_d$ (m) | Reference |
|---|---|---|---|---|
| Field measurements | — | 0.23 | 15 ~ 20 | Estimated from Fig. 8 |
| Numerical results | — | 0.20 | 15 ~ 20 | — |
| Analytical solutions | Benjamin (1968) $C = 0.7$ from Eq. (6) | 0.28 | 12.7 | $U_d$ from Eq. (5); $h_d$ from Eq. (8) |
| | Kao (1977) $C = 1.4$ from Eq. (7) | 0.19 | 18.6 | $U_d$ from Eq. (5); $h_d$ from Eq. (8) |

**Table 2.** Calculated Plunge Depth of the Turbid Density Currents

| Peak inflow (Q) ($m^3/s$) | W (m) | $\rho_a$ ($kg/m^3$) | $\rho_d$ ($kg/m^3$) | $F_p$ [Eq. (32)] | $h_p$ [Eq. (31)] (m) | Simulation ($h_p$) (m) |
|---|---|---|---|---|---|---|
| 2,650 | 500 | 997.3 | 999.3 | 0.43 | 20 | 20 ~ 25 |

## Parametric Analysis

A parametric analysis was performed to gain further insights into interflow propagation dynamics at Imha Reservoir. To assist the reservoir operators, the influence of three important parameters were investigated: (1) sediment particle size; (2) sediment concentration; and (3) seasonal reservoir stratification. This analysis would help answer questions relevant to what would happen for different concentration and particle size distribution of the inflows and what type of density current would be observed for typhoons during different time of the year.

### *Influence of Sediment Particle Size*

Numerous simulations were carried out with various particle sizes, whereas all other parameters were identical to the field measurements during Typhoon Ewiniar. The properties measured along the thermocline level (EL. 125.0 ~ 135.0 m) are of primary significance in this analysis. To display the results in dimensionless form, the sediment delivery ratio $C_o/C_i$ is defined as the ratio of the outflow sediment concentration (delivered in suspension to the dam wall G4) to the inflow sediment concentration at the inlet point (G2). Fig. 14 shows the sediment delivery ratio decreasing primarily with increasing particle size, which demonstrates the sediment particle size effect on interflow dynamics. For particle sizes $d_s$ less than 10 $\mu$m, the delivery ratio is 1.0 and the incoming sediment concentration from the reservoir inlet (G2) will be transported without concentration reduction because of sediment deposition. A suspended regime is defined when particles are finer than $d_s < 10$ $\mu$m and settling is negligible. Numerical simulations in the suspended regime can be carried out with a homogeneous fluid without significant particle settling. Particle settling becomes increasingly dependent on particle size, and a transition regime is obtained where particle sizes $10 < d_s < 40$ $\mu$m. When the particle sizes $d_s$ are greater than 40 $\mu$m, they will rapidly settle without forming density currents. The turbid inflows entering the reservoir may consist of

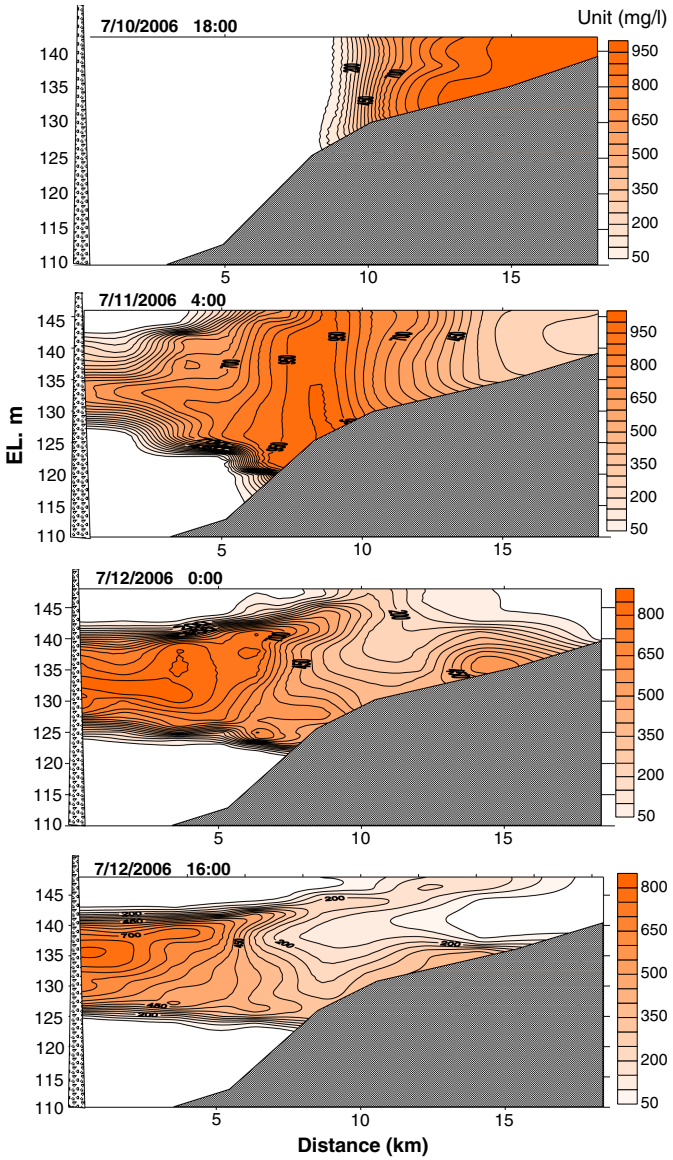


**Fig. 13.** Longitudinal profile of suspended sediment concentration (mg/L); contours ranging from 50 to 1,000 mg/L in increments of 50 mg/L

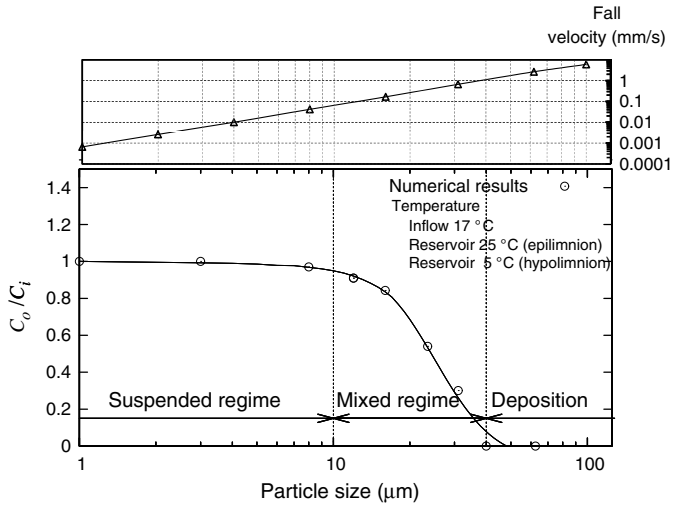


**Fig. 14.** Sediment delivery ratio ($C_o/C_i$) as a function of particle size; $C_i$ = inflow sediment concentration from the inlet point (G2); $C_o$ = outflow sediment concentration horizontally transported to Imha Dam (G4) along the thermocline (EL. 125.0 ~ 135.0 m); fall velocity of particles is found in Julien (2010)

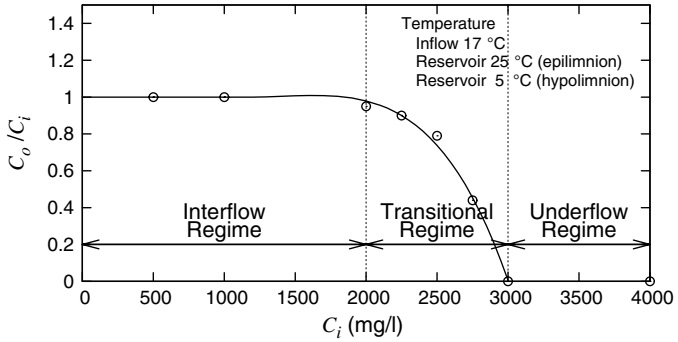


**Fig. 15.** Propagation types of turbid density currents, classified into three flow regimes based on incoming sediment concentrations; $C_o$ = sediment concentration horizontally transported to Imha Dam (G4) along the thermocline (EL. 125.0 ~ 135.0 m)

various particle sizes. When they pass through the riverine or transitional zone shown in Fig. 7, the coarse particles settle through the riverine or transitional zone, and only very small size particles can be transported to the dam wall through the lacustrine zone. Thus, the horizontally intrusive turbidity currents in the interflow regime will only contain particle sizes finer than 40 $\mu$m, which is confirmed with the field observations in the reservoir shown in Fig. 5.

### *Influence of Sediment Concentration*

When river inflows containing high concentrations of fine sediments enter a reservoir, the concentration is expected to influence the formation type and the propagation dynamics of density currents. Numerical simulations were performed to evaluate the response of density flows to the changes of incoming sediment concentration from G2. The sediment inflows were assumed to consist of only very small size particles (less than 5.0 $\mu$m) in the suspended regime such that settling would not interfere with the results. The inflows and associated temperature entering the reservoir at G2 were specified to be equal to the field measurements during Typhoon Ewiniar. The initial thermal stratification of the reservoir was also specified to be identical to the temperature profile measured on July 10, 2006. Fig. 15 presents three flow regimes determining the intrusion types of density currents: (1) interflows when the sediment concentration $C_i$ is less than 2,000 mg/L; (2) a transitional regime with multiple intrusions (i.e., interflows and underflows) when $2{,}000 < C_i < 3{,}000$ mg/L; and (3) plunging underflows when $C_i$ is greater than 3,000 mg/L. Multiple intrusions (i.e., interflows and undeflows) were sometimes observed in the field (K-water 2006). These threshold values (2,000 and 3,000 mg/L) can be used to practically predict the occurrence of turbid density currents, propagation type, and intrusion level in Imha Reservoir.

### *Influence of Seasonal Stratification*

Also explored were the effects of seasonal thermal stratification on turbid density currents in the reservoir. Only fine particles in the suspended regime are considered to eliminate the effects of particle settling and to highlight the effects of thermal stratification. Fig. 16

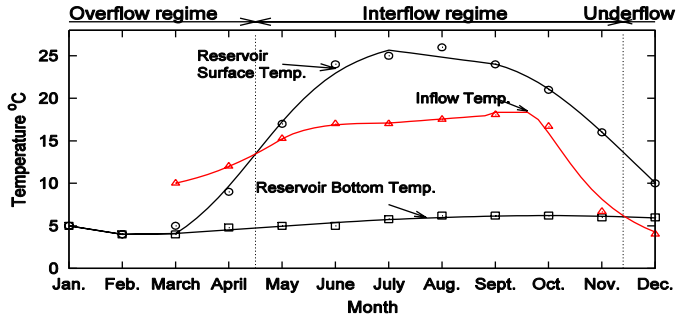


**Fig. 16.** Seasonal variation in the temperature of inflows and the reservoir, measured during 2006

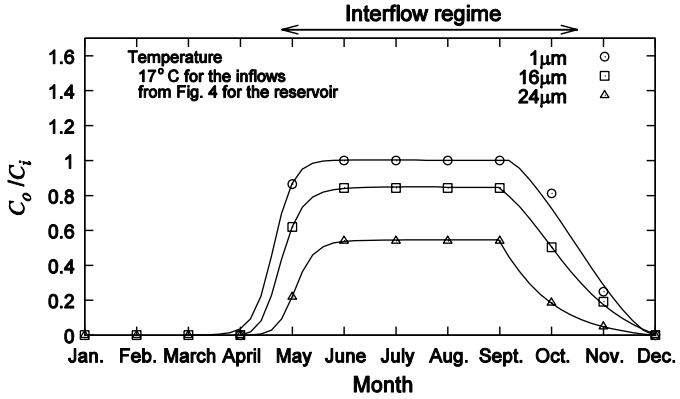


**Fig. 17.** Effect of seasonal variations of thermal structure in the reservoir and inflow temperature on the turbid density currents; $C_i$ = sediment concentration of inflows entering the reservoir; $C_o$ = outgoing sediment concentration horizontally transported to Imha Dam (G4) along the thermocline (EL. 125.0 ~ 135.0 m)

demonstrates the seasonal variation between the inflow temperatures and reservoir temperatures during 2006. The temperatures of the reservoir were monthly averaged values, whereas the inflow temperatures were measured right after rainfall events. Numerical simulations were carried out considering the monthly thermal structure of the reservoir (Fig. 4) and the monthly temperature of the river inflows based on field measurements from 2006. The river inflows and sediment loads for the numerical simulations were identical to the conditions during Typhoon Ewiniar. Numerical results shown in Fig. 17 demonstrate that the summer stratification is strongly connected with the formation of turbid interflows in Imha Reservoir. Comparatively, winter conditions typically produce underflows without turbidity problems, and spring conditions may develop either overflows at very low sediment concentrations and underflows at high concentrations.

## Conclusions

A detailed 3D modeling analysis of the propagation dynamics of turbid density currents in Imha Reservoir, South Korea has been presented. The main conclusion is that the particle dynamics algorithm coupled with the 3D numerical model appropriately simulates the propagation dynamics of the density currents with particle settling at Imha Reservoir. The coupled nonhydrostatic FLOW-3D numerical model has been calibrated and tested during Typhoon Ewiniar in 2006. The turbidity modeling was successfully validated against field measurements of water temperature and turbidity.

The analysis of the effects of particle size on interflow propagation dynamics indicates that the turbid density currents belong to the suspended regime and settling is not significant when $d_s < 10$ $\mu$m. For sediment particles coarser than 40 $\mu$m, settling becomes dominant and density currents vanish. The particle dynamics algorithm is essential to properly simulate turbid density currents with particle sizes $10 < d_s < 40$ $\mu$m.

The simulation results also demonstrate that the river inflows will form interflows during the summer months when the inflowing sediment concentration $C_i < 2{,}000$ mg/L. At inflow concentrations $C_i$ greater than 3,000 mg/L, density currents will plunge and propagate as underflows. Therefore, highly concentrated turbid interflows are not expected to occur when $C_i$ exceeds the threshold value of 3,000 mg/L. It was also shown that the summer stratification is strongly connected with the formation of interflows in the reservoir. This parametric study defines the range of sediment size and concentration ($10 < d_s < 40$ $\mu$m and $2{,}000 < C_i < 3{,}000$ mg/L) for which density currents are expected to be a concern at Imha Reservoir.

## Acknowledgments

This study was completed during the Ph.D. studies of the first author at Colorado State University. The financial support from the Korea Water Resources Corporation (K-water) is gratefully acknowledged.

## Notation

*The following symbols are used in this paper:*

$A$ = fractional area, open to flow in FAVOR method;
$A_d$ = cross-sectional area of the density current;
$A_s$ = surface area of the reservoir;
$C$ = density current coefficient;
$C_i$ = inflow sediment concentration;
$C_o$ = outflow sediment concentration;
$c_\mu$, $c_{1\varepsilon}$ = empirical turbulence constants;
$c_{2\varepsilon}$, $c_{3\varepsilon}$ = empirical turbulence constants;
$d_s$ = particle diameter;
$d_{50}$ = average median grain size;
$E$ = entrainment coefficient;
$\mathrm{F}_p$ = densimetric Froude number at a plunge point;
$f_b$ = bed friction;
$f_i$ = interfacial friction;
$G$ = constant specific gravity of sediment particles;
$g'$ = reduced gravity
$g_i$ = gravitational acceleration components in each direction;
$H$ = total reservoir flow depth;
$h_d$ = intrusive depth of a density current;
$h_p$ = plunge depth;
$i, j, k$ = cell indices in $x-$, $y-$, $z-$ directions
$L$ = reservoir length;
$M_N$ = field measurements;
$N$ = number of data;
$n$ = time level;
$p$ = total pressure;
$Q_i$ = inflow discharge of a density current;
$Q_o$ = outflow discharge at the dam;
$q_o$ = unit discharge for a rectangular channel;
$\mathrm{Sc}t$ = turbulent Schmidt number;

$S_{ij}$ = strain rate tensor;
$S_N$ = simulation results;
$S_o$ = bed slope;
$t$ = time;
$U_d$ = depth-averaged propagation speed of a density current;
$u_i$ = mean velocity components in a Cartesian coordinate system ($x$, $y$, $z$);
$u, v, w$ = horizontal ($x-$, $y-$ direction) and vertical ($z-$ direction) water mean velocity;
$-\overline{u_i' u_j'}$ = Reynolds stresses;
$-\overline{u_i' \phi'}$ = turbulent fluxes of the scalar $\phi$;
$u_*$ = shear velocity;
$V_f$ = fractional volume, open to flow in FAVOR method;
$V^n_{s_{ijk}}$ = volume of solid particles in the cell ($i$, $j$, $k$);
$V^n_{ijk}$ = total fluid volume in the cell ($i$, $j$, $k$);
$W$ = reservoir width;
$\beta$ = turbulence parameter;
$\Gamma$ = molecular diffusivity of the scalar $\phi$;
$\Gamma_t$ = turbulent (eddy) scalar diffusivity defined as $\Gamma_t = \nu_t / \mathrm{Sc}_t$;
$\delta_{ij}$ = Kronecker delta;
$\varepsilon$ = turbulence kinetic energy dissipation rate;
$k$ = turbulent kinetic energy;
$\eta_o$ = ratio of the turbulent time scale to the mean strain time scale;
$\nu$ = fluid kinematic viscosity;
$\nu_t$ = turbulent (eddy) viscosity;
$\phi$ = passive scalar;
$\Delta\rho$ = mass density difference between ambient fluid and a density current;
$\rho_d$ = mass density of the density current;
$\rho_L$ = fluid mass density of a lower layer;
$\rho_r$ = reference fluid mass density;
$\rho_U$ = fluid mass density of an upper layer;
$\rho_w(T)^n_{ijk}$ = water density in a cell at temperature $T$ in °C;
$\sigma_k$ = empirical turbulence diffusion constant;
$\sigma_\varepsilon$ = empirical dissipation constant; and
$\omega_s$ = particle settling velocity.

## References


An, S. D. (2011). "Interflow dynamics and three-dimensional modeling of turbid density currents in Imha Reservoir, South Korea." Ph.D. dissertation, Dept. of Civil and Environmental Engineering, Colorado State Univ., Fort Collins, CO, 166.

An, S. D., Julien, P. Y., and Venayagamoorthy, S. K. (2012). "Numerical simulation of particle-driven gravity currents." *Environ. Fluid Mech.*, 12(6), 495–513.

Balistrieri, L., Tempel, R., Stillings, L., and Shevenell, L. (2006). "Modeling spatial and temporal variations in temperature and salinity during stratification and overturn in Dexter Pit Lake, Tuscarora, Nevada, USA." *Appl. Geochem.*, 21(7), 1184–1203.

Bell, V., George, D., Moore, R., and Parker, J. (2006). "Using a 1-D mixing model to simulate the vertical flux of heat and oxygen in a lake subject to episodic mixing." *Ecol. Model.*, 190(1–2), 41–54.

Benjamin, T. B. (1968). "Gravity currents and related phenomena." *J. Fluid Mech.*, 31(2), 209–248.

Çalışkan, A., and Elçi, Ş. (2009). "Effects of selective withdrawal on hydrodynamics of a stratified reservoir." *Water Resour. Manage.*, 23(7), 1257–1273.

Chen, X. (2005). "A comparison of hydrostatic and nonhydrostatic pressure components in seiche oscillations." *Math. Comput. Model.*, 41(8–9), 887–902.

Chen, Y. J. C., Wu, S. C., Lee, B. S., and Hung, C. C. (2006). "Behavior of storm-induced suspension interflow in subtropical Feitsui Reservoir, Taiwan." *Limnol. Oceanogr.*, 51(2), 1125–1133.

Cheng, R. T., and Casulli, V. (2001). "Evaluation of the UnTRIM model for 3-D tidal circulation." *Proc., 7th Int. Conf. on Estuarine and Coastal Modeling*, ASCE, Reston, VA, 628–642.

Chikita, K., and Okumura, Y. (1990). "Dynamics of turbidity currents measured in Katsurazawa Reservoir, Hokkaido, Japan." *J. Hydrol.*, 117(1–4), 323–338.

Chung, S. W., and Gu, R. (1998). "Two-dimensional simulations of contaminant currents in stratified reservoir." *J. Hydraul. Eng.*, 10.1061/(ASCE)0733-9429(1998)124:7(704), 704–711.

Chung, S. W., Hipsey, M. R., and Imberger, J. (2009). "Modelling the propagation of turbid density inflows into a stratified lake: Daecheong Reservoir, Korea." *Environ. Model. Software*, 24(12), 1467–1482.

Cole, T. M., and Wells, S. A. (2006). "CE-QUAL-W2: A two-dimensional, laterally averaged, hydrodynamic and water quality model." *Version 3, Instruction Rep. EL-06-01*, Vicksburg, MS.

De Cesare, G., Boillat, J. L., and Schleiss, A. J. (2006). "Circulation in stratified lakes due to flood-induced turbidity currents." *J. Environ. Eng.*, 10.1061/(ASCE)0733-9372(2006)132:11(1508), 1508–1517.

De Cesare, G., Schleiss, A., and Hermann, F. (2001). "Impact of turbidity currents on reservoir sedimentation." *J. Hydraul. Eng.*, 10.1061/(ASCE)0733-9429(2001)127:1(6), 6–16.

Fang, X. (2004). "Simulation of thermal/dissolved oxygen habitat for fishes in lakes under different climate scenarios: Part 1. Cool-water fish in the contiguous US." *Ecol. Model.*, 172(1), 13–37.

*FLOW-3D* [Computer software]. (2007). *User guide and manual release 9.3*, Flow Science, Santa Fe, NM.

Ford, D. E., and Johnson, M. C. (1983). "An assessment of reservoir density currents and inflow processes." *Technical Rep. E-83-7*, U.S. Army Corps of Engineers, Waterways Experiment Station, Vicksburg, MS.

Fringer, O. B., Gerritsen, M. G., and Street, R. L. (2006). "An unstructured-grid, finite-volume, nonhydrostatic, parallel coastal ocean simulator." *Ocean Model.*, 14, 139–173.

Gill, A. E. (1982). *Atmosphere-ocean dynamics*, Academic Press, New York.

Gladstone, C., Phillips, J. C., and Sparks, R. S. J. (1998). "Experiments on bidisperse, constant-volume gravity currents propagation and sediment deposition." *Sedimentology*, 45(5), 833–843.

Gosink, J. (1987). "Northern lake and reservoir modeling." *Cold Regions Sci. Tech.*, 13(3), 281–300.

Hamrick, J. M. (1992). "A three-dimensional environmental fluid dynamics computer code: Theoretical and computational aspects." *Special Rep. 317*, College of William and Mary, Virginia Institute of Marine Science, Williamsburg, VA.

Hirt, C. W., and Nichols, B. D. (1981). "Volume of fluid (VOF) method for the dynamics of free boundaries." *J. Comput. Phys.*, 39, 201–225.

Hodges, B., and Dallimore, C. (2007). *Estuary, lake and coastal ocean model: ELCOM v2.2 user manual*, Centre for Water Research, Univ. of Western Australia, Crawley, Australia.

Hodges, B. R. (2009). "Hydrodynamical modeling." *Encyclopedia of Inland Waters*, G. E. Likens, ed., Elsevier, Oxford, U.K.

Howard, C. S. (1953). "Density currents in Lake Mead." *Proc., 5th IAHR Congress, International Association for Hydraulic Research*, International Association for Hydraulic Research, Madrid, Spain, 335–368.

Ji, U., Julien, P. Y., and Park, S. K. (2011). "Sediment flushing at the Nakdong river estuary barrage." *J. Hydraul. Eng.*, 10.1061/(ASCE)HY.1943-7900.0000395, 1522–1535.

Julien, P. Y. (2010). *Erosion and sedimentation*, Cambridge University Press, Cambridge, U.K., 371.

Kao, T. (1977). "Density currents and their applications." *J. Hydraul. Div.*, 103(5), 543–555.

Keulegan, G. H. (1957). "Thirteenth progress report on model laws for density currents an experimental study of the motion of saline water from locks into fresh water channels." *Standards Rep. 5168*, U.S. National Bureau of Standards, Washington, DC.

Kim, H. S., and Julien, P. Y. (2006). "Soil erosion modeling using RUSLE and GIS on the Imha watershed." *Water Eng. Res.*, 7(1), 29–41.

K-water. (2006). *Field measurements of turbid density currents in Soyang Reservoir, technical note*, Korea Water Resources Corporation, Daejeon, Korea (in Korean).
K-water. (2007). *Investigation of the relationship between turbid water and water quality in Imha Reservoir, technical note*, Korea Water Resources Corporation (in Korean).
Laval, B., Imberger, J., Hodges, B. R., and Stocker, R. (2003). "Modeling circulation in lakes: Spatial and temporal variations." *Limnol. Oceanogr.*, 48(3), 983–994.
Lee, G., and Cho, G. (2004). "Evaluation of GIS-based soil erosion amount with turbid water data." *Korean Soc. Geospatial Inform. Syst.*, 12(4), 75–81.
Lee, S., Kim, J., Noh, J., and Ko, I. H. (2007). "Assessment of selective withdrawal facility in the Imha reservoir using CE-QUAL-W2 model." *J. Korean Soc. Water Qual.*, 23(2), 228–235 (in Korean).
Middleton, G. V. (1966). "Experiments on density and turbidity currents: I. Motion of the head." *Can. J. Earth Sci.*, 3(5), 627–637.
Morris, G. L., and Fan, J. (1998). *Reservoir sedimentation handbook*, McGraw-Hill, New York.
Oehy, C., and Schleiss, A. J. (2007). "Control of turbidity currents in reservoirs by solid and permeable obstacles." *J. Hydraul. Eng.*, 10.1061/(ASCE)0733-9429(2007)133:6(637), 637–648.
Pope, S. B. (2000). *Turbulent flows*, Cambridge University Press, Cambridfe, U.K., 771.
Rodi, W. (1980). *Turbulence models and their application in hydraulics—A state of the art review*, International Association of Hydraulic Research, Madrid, Spain, 44–46.
Savage, S. B., and Brimberg, J. (1975). "Analysis of plunging phenomena in water reservoirs." *J. Hydraul. Res.*, 13(2), 187–205.
Sutherland, B. R., Kyba, P. J., and Flynn, M. R. (2004). "Intrusive gravity currents in two-layer fluids." *J. Fluid Mech.*, 514, 327–353.
Umeda, M., Yokoyama, K., and Ishikawa, T. (2006). "Observation and simulation of floodwater intrusion and sedimentation in the Shichikashuku reservoir." *J. Hydraul. Eng.*, 10.1061/(ASCE)0733-9429(2006)132:9(881), 881–891.
Venayagamoorthy, S. K., and Stretch, D. D. (2010). "On the turbulent Prandtl number in homogeneous stably stratified turbulence." *J. Fluid Mech.*, 644, 359–369.
Wadzuk, B. M., and Hodges, B. R. (2004). "Hydrostatic and nonhydrostatic internal wave models." *CRWR Online Rep. 04-09*, Univ. of Texas, Austin, TX.
Weilbeer, H., and Jankowski, J. (2000). "A three-dimensional nonhydrostatic model for free surface flows–Development, verification and limitations." *Proc., 6th Int. Conf. Estuarine and Coastal Modeling*, ASCE, Reston, VA, 162–177.
Williams, N. (2007). "Modeling dissolved oxygen in Lake Powell using CE-QUAL-W2." M.S. thesis, Brigham Young Univ., Provo, UT.
Yakhot, V., Orszag, S. A., Thangam, S., Gatski, T. B., and Speziale, G. G. (1992). "Development of turbulence models for shear flows by a double expansion technique." *Phys. Fluids*, 4(7), 1510–1520.
Yi, Y., Kim, Y. D., Park, K., and Kim, W. (2005). "Two dimensional numerical modeling of turbidity variation in Imha reservoir." *Korean Soc. Civ. Eng.*, 25(4B), 237–334 (in Korean).